Organic Electronics 15 (2014) 2677–2684

Contents lists available at ScienceDirect

Organic Electronics

journal homepage: www.elsevier.com/locate/orgel

Flexible organic phototransistors based on a combination of printing methods

Minseok Kim [a], Hyun-Jun Ha [a], Hui-Jun Yun [b], In-Kyu You [c], Kang-Jun Baeg [d,1], Yun-Hi Kim [b,1], Byeong-Kwon Ju [a,*]

[a] Display and Nanosystem Laboratory, College of Engineering, Korea University, Seoul 136-713, Republic of Korea
[b] Department of Chemistry, Research Institute of Nature Science (RINS), Gyeongsang National University, Jinju 660-701, Republic of Korea
[c] Convergence Components & Materials Research Laboratory, Electronics and Telecommunications Research Institute (ETRI), Daejeon 305-700, Republic of Korea
[d] Nanocarbon Materials Research Center, Creative and Fundamental Research Division, Korea Electrotechnology Research Institute (KERI), Changwon, Gyeongsangnamdo 642-120, Republic of Korea

ARTICLE INFO

Article history:
Received 2 April 2014
Received in revised form 28 July 2014
Accepted 30 July 2014
Available online 13 August 2014

Keywords:
Organic phototransistors
Printed electronics
Reverse offset printing
Organic semiconductors
Field-effect transistors

ABSTRACT

Highly photosensitive organic phototransistors (OPTs) are successfully demonstrated on a flexible substrate using all-solution process as well as a combination of printing methods which consist of roll-to-plate reverse offset printing (ROP), inkjet printing and bar coating. Excellent electrical switching characteristics are obtained from heterogeneous interfacial properties of the reverse-offset-printed silver nanoparticle electrode and the inkjet-printed *p*-channel polymeric semiconductor. In particular, the OPTs exhibit remarkably photosensitivity with a photo-to-dark current ratio exceeding 5 orders. This optoelectronic properties of the combinational printed OPTs are theoretically and experimentally studied, and found the comparable tendency. In addition, excellent mechanical stability is observed with up to 0.5% of strain applied to the OPTs. Hence, by manufactured with a combination of various graphic art printing methods such as roll-to-plate ROP, inkjet printing, and bar coating, these devices are very promising candidates for large-area and low-cost printed and flexible optoelectronics applications.

1. Introduction

Recently, organic photo detectors based on π-conjugated molecules have remarkably been attracted as devices for optical communications, digital imaging, and sensing [1]. The optoelectronic properties (i.e., charge generation, transport, and recombination) of organic semiconductors can be relatively easily tunable by controlling their molecular structures; these semiconductors generally exhibit excellent photocurrent generation efficiency [2,3]. The spectral sensitivity of the organic active materials can also be modified to either be panchromatic or selectively tuned to a specific wavelength from ultraviolet to near infrared (NIR) regions [3]. Moreover, the low-temperature and solution processability of the functional organic materials as well as soft mechanical properties allow for their use in a variety of innovative light-signal detection systems such as large-area imagers and scanners, NIR or X-ray detection in bio-medical applications, short-range plastic optical-fiber-based transceivers, position-sensitive detectors, and integrated sensoristics for Lab-on-a-chip [4].

Organic phototransistors (OPTs) are a type of photo detector device in which the incident light signal can modulate the charge-carrier density in the active channel of organic field-effect transistors (OFETs), thereby changing

* Corresponding author.
E-mail addresses: kangjun100@keri.re.kr (K.-J. Baeg), ykim@gnu.ac.kr (Y.-H. Kim), bkju@korea.ac.kr (B.-K. Ju).
[1] Co-corresponding authors.

http://dx.doi.org/10.1016/j.orgel.2014.07.041
1566-1199/

the channel conductance. Compared to conventional photodiodes, the OPTs are able to detect the light signal more sensitively without serious problems such as noise increment, and they are easily interpretable into electronic circuitry because of their complementary metal oxide semiconductor (CMOS) like configuration. To this end, a number of π-conjugated organic molecules, including vacuum-deposited or solution-processed small molecular semiconductors and polymers, are widely applied [4–6].

Graphic art printing (GAP) methods, such as screen [7], bar coating [8], inkjet [9], flexographic [10], gravure [11], offset [12], and spray [13], are more simply able to form a patterned layer compared with conventional photolithography and lift-off processes. Organic optoelectronic devices, including OPTs manufactured by GAPs, have attracted significant interest because of their potential to set a new paradigm in the fabrication process of low-cost, large-area, and flexible devices: displays [14], photovoltaics [15], flash memories [16], and radio frequency identification tags [17]. Previous research has focused on conventionally processed optical devices, so there has been a lack of studies on flexible optoelectronics based on the printing techniques. A few of the light-responsive OPTs have been used to partially solution-processed and/or inkjet-printed organic photo-active semiconductor on rigid substrate [18,19].

We reported previously heterogeneous interfacial properties between the reverse-offset-printed silver (Ag) source/drain (S/D) and spin-coated *p*-channel organic semiconductor on glass substrate [20]. Herein, we report optoelectronic properties of highly photosensitive flexible OPTs based on a combination of printing methods. Sequential printing processes of reverse offset printing (ROP) for Ag S/D electrodes, inkjet printing for an active semiconductor layer, bar coating for polymer gate dielectrics, and inkjet-printed conductive polymer for gate electrodes facilitate the fabrication of cost-effective large-area, flexible, organic image sensors and scanners. We examine both theoretically and experimentally the optoelectronic properties of the flexible OPTs manufactured by a combination of printing methods. The mechanical bending properties are also characterized for the flexible devices.

2. Experimental

The Ag S/D electrodes were fabricated by roll-to-plate reverse offset printing (ROP). Ag nanoparticle pastes (Ag content: 39 wt%, viscosity: 1.5 cPs at 0.4 rpm, surface tension: 25.8 mN m^{-1}; ANP Co.) were dispensed under the control of a syringe pump onto the surface of the polydimethylsiloxane (PDMS) blanket roll. The PDMS-covered blanket was rolled over the cliché which is printing plate with intaglio patterns, and then the extra ink was eliminated from the blanket and transferred onto the top of the cliché surface. The remaining Ag paste, which was in the desired pattern on the blanket, was transferred onto plastic or glass substrates. For a cliché with intaglio patterns, a 6-in. Si wafer was patterned by photolithography and a deep reactive ion-etching process. To remove the various additives and residual solvents in the printed Ag paste, the substrates were thermally cured at various temperatures on a hotplate for 20 min in air. The substrates were then cleaned with deionized water, acetone, and isopropyl alcohol for 10 min each, sequentially. The polymer semiconductor poly[2,5-bis(2-octyldodecyl)pyrrolo[3,4-c]pyrrole-1,4(2H,5H)-dione-(E)-1,2-di(2,2′-bithiophen-5-yl)ethene] (PDPP-DBTE) was synthesized [21], and dissolved in dichlorobenzene to obtain a 6 mg/ml solution. The inkjet-printed PDPP-DBTE films were formed using a 50 μm orifice diameter piezoelectric-type single nozzle (Microfab, Inc.) in air, after which they were thermally annealed at various temperatures for 30 min in an Ar-purged glove box. As a gate dielectric layer, poly(methyl methacrylate) (PMMA) (Sigma Aldrich, MW = 120 k, dielectric constant ε_r = 3.5) was dissolved in n-butyl acetate (nBA) (120 mg ml^{-1}), and the solution was bar-coated (thickness = ~1.2 μm). The film was then baked at 100 °C for 30 min in the same glove box to remove residual solvent. The top-gate/bottom-contact (TG/BC) structure of the OPTs was completed with the formation of the gate electrode using the inkjet printer (UJ200MF, Unijet, Korea) of a conducting polymer poly(3,4-ethylenedioxythiophene): poly(styrenesulfonate) (PEDOT:PSS) (Clevios PH1000, H.C. Starck). The PEDOT:PSS was thermally annealed on a hotplate at 80 °C for 2 h in the Ar-purged glove box.

3. Results and discussion

The OPTs were fabricated monolithically on a flexible substrate via a combination of various printing processes, as shown in Fig. 1a. At first, S/D electrodes (using Ag nanoparticle paste) were printed by a roll-to-plate reverse offset printing technique, which can easily produce complicated and fine S/D electrode patterns on a scale of approximately 20 μm in line and space. The complicated and fine comb-pattern electrode with short channel length of 20 μm was designated for high integration as well as the high switching property. As the channel length was decreased, mobility was decreased revealing serious contact resistance of short channel OFETs. Polymeric semiconductor, PDPP-DBTE, as a photo-active channel layer was then formed by a drop-on-demand inkjet printing process onto the Ag S/D electrodes [channel width/length (W/L) = 1000 μm/20 μm]. Fig. 1b and c shows the chemical structure of the PDPP-DBTE polymer semiconductor and its inkjet-printed features, respectively [21]. A polymer gate dielectric layer, PMMA, is then deposited by bar coating onto the active layer [8]. As a top-gate electrode, PEDOT:PSS conducting polymer was finally formed by the inkjet printing method, as shown in Fig. 1d. The digital camera image of flexible OPTs (6 × 6 phototransistor array), which was formed on a transparent and colorless polyimide (PI) plastic substrate, is shown in Fig. 1e.

The typical transfer (drain current I_D vs. gate voltage V_G) and output (I_D vs. drain voltage V_D) characteristics of the flexible PDPP-DBTE OFETs fabricated by a combination of printing methods are shown in Fig. 1f and g, respectively. According to the gradual channel approximation and its common equation for FETs in the saturation regime (at

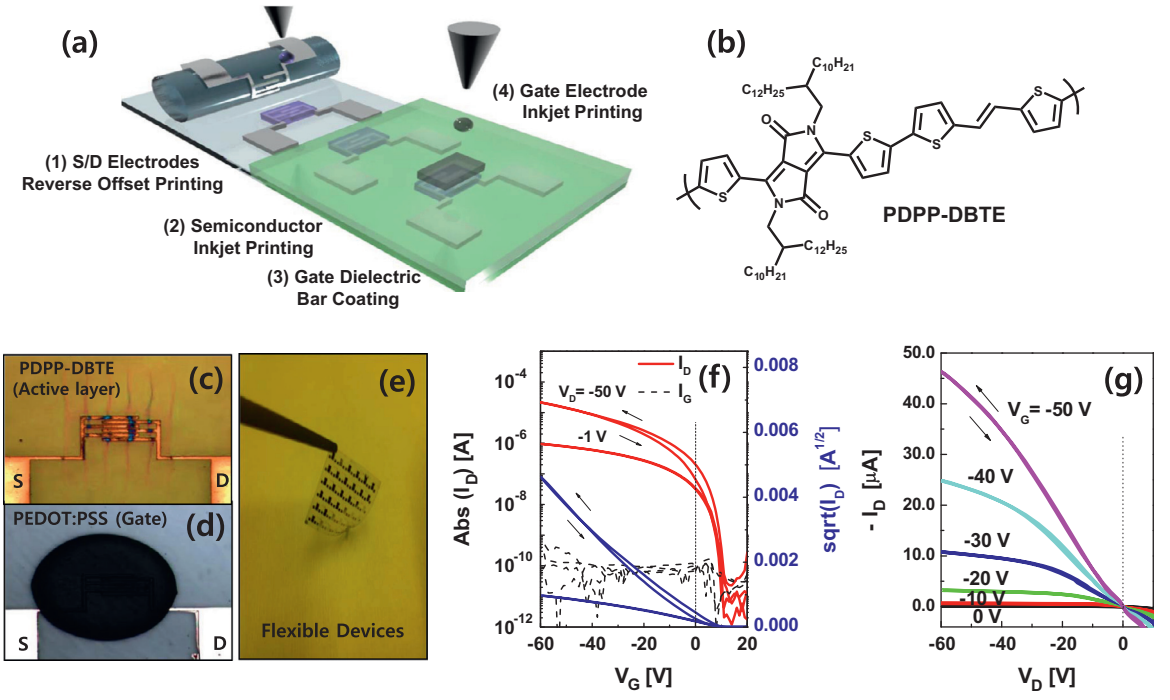

Fig. 1. (a) Schematic process flow for fabrication of OPTs based on combination of printing methods. (b) Chemical structure of PDPP-DBTE polymer semiconductor. Digital camera images of (c) inkjet-printed polymer semiconductor on reverse-offset-printed Ag S/D electrodes, (d) inkjet-printed conductive polymer gate electrode, and (e) flexible devices on plastic substrate. Typical current–voltage characteristics of the flexible PDPP-DBTE OFET devices: (f) transfer (I_D vs. V_G) and (g) output (I_D vs. V_D) plots.

$V_D < V_G - V_T$), fundamental device parameters such as the field-effect mobility (μ_{FE}), threshold voltage (V_T), ON-/OFF-current ratio (I_{on}/I_{off}), and subthreshold swing (SS) were evaluated at $V_D = -50$ V. Those device parameters were obtained at a different thermal annealing temperature of the PDPP-DBTE semiconductor films from 100 to 200 °C, and were extracted in Table 1. We found that the *p*-channel PDDP-DBTE OFETs exhibited the best performance under the annealing temperature of 180 °C, where μ_{FE} and V_T were approximately 0.26 cm^2 V^{-1} s^{-1} [0.68 cm^2 V^{-1} s^{-1}] and −11.9 V [−16.6 V] at W/L = 1000 μm/20 μm [1000 μm/10 μm], respectively. This was attributed to the enhanced π–π stacking of highly π-extended polymer backbones and higher-ordered crystalline phase via high-temperature thermal treatment [22].

To measuring the electrical conductivity of printed Ag electrode, the Ag nanoparticle paste was spin-coated on glass substrates, and cured at different temperatures on hotplate in air. The electrical conductivity was calculated from the thickness and the sheet resistance using the four-point probe method. As seen in Fig. 2a, the initial Ag nanoparticle film showed very low conductivity of approximately 1.0×10^{-5} S cm^{-1} at the thermal curing temperature of 150 °C, whereas showed a dramatically increased high conductivity with approximately 2.0×10^5 S cm^{-1} at up to 200 °C of curing temperature. More than 200 °C, the experimentally measured electrical conductivity value is quite similar to that of bulk Ag (approximately 6.17×10^5 S cm^{-1}). The insert images in Fig. 2a are the as-distributed Ag nanoparticles in paste and selected area electron diffraction pattern of the spherical Ag nanoparticles from the high resolution transmission electron microscopy (HRTEM). Nano-sized Ag particles with less than 10 nm allow the metallic property of printed Ag electrode at low-temperature of 200 °C.

The surface roughness of the Ag nanoparticle film on a glass substrate was characterized by the atomic force microscopy (AFM). As seen in Fig. 2b, as-printed Ag nanoparticle showed a minimum root mean square roughness (R_q) with approximately 9.8 nm, and gradually increased to 29.1 nm as curing temperature increased with 350 °C, At more than an excessively high curing

Table 1
Transistor parameters for PDPP-DBTE OFETs at different thermal annealing temperatures.

Active materials	Annealing temperature (°C)	μ_{FE} (cm^2 V^{-1} s^{-1})	V_T (V)	I_{on}/I_{off}	SS (V Dec.$^{-1}$)
PDPP-DBTE	100	0.14	−2.29	~10^5	−1.99
	140	0.14	−3.39	~10^5	−2.55
	180	0.26	−11.88	~10^5	−2.49
	200	0.16	−7.14	~10^5	−3.82

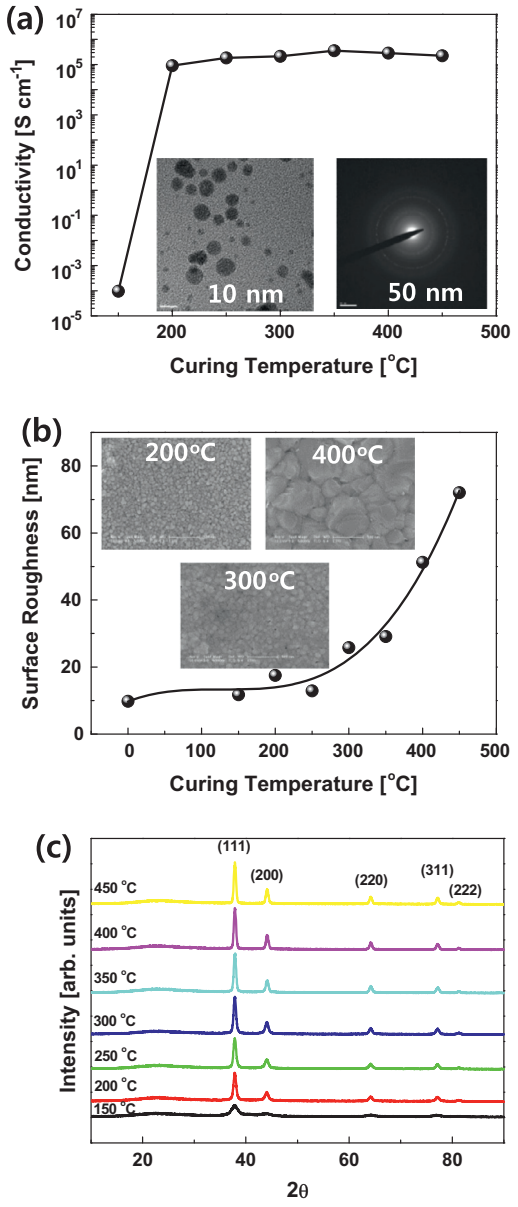

Fig. 2. Properties of Ag nanoparticle electrode cured at different thermal temperatures on a glass substrate. (a) Electrical conductivity. The inset shows TEM images of spherical Ag nanoparticles and its selected area electron diffraction (SAED) pattern. (b) Surface roughness. The inset shows topological SEM images in scale of 500 nm. (c) XRD spectra that indicate the face-centered-cubic (FCC) lattice structure (111), (200), (220), (311) and (222) crystal plane of Ag metal.

temperature with 450 °C, R_q exponentially increased to 72.04 nm because of the agglomeration of Ag nanoparticles. Insert images in Fig. 2b are the top surface morphology of the Ag nanoparticle film from the scanning electron microscope (SEM), which gradually grew into large crystalline grains as the curing temperature increases. Additionally, this result is confirmed by using the X-ray diffraction (XRD) spectra which are corresponding to the face-centered-cubic (FCC) lattice structure (111), (200), (220), (311) and (222) crystal plane of bulk Ag metal, as shown in Fig. 2c [23].

The Fermi level of the printed Ag electrode was evaluated using ultraviolet photoelectron spectroscopy (UPS). As shown in Fig. 3, the work function (Φ) of the metal electrode is obtained by measuring the width of the emitted electrons (W_e) from the onset of the secondary electrons up to the Fermi edge and subtracting W_e from the energy of the incident UV light ($h\nu$) with 21.22 eV photons (He I line), as follows: $\Phi = h\nu - W_e$. We obtained the Φ values of the ROP Ag electrodes; they were approximately −3.10, −5.09, −4.96, −4.97 and −5.14 eV at thermal curing temperatures of 150, 200, 250, 300 and 350 °C, respectively. In comparison with Φ of bulk Ag ($\Phi = -4.5$ eV), the relatively higher Φ of the printed Ag electrodes was mostly attributed to the formation of silver oxide, as verified by X-ray photoemission spectroscopy (XPS). As shown in Fig. 4, The peaks at 368 and 532 eV denote the core level of a silver (the 3d orbital) and oxygen atoms (the 1s orbital), respectively, which showed considerably large intensity with increasing cuting temperatures of Ag nanoparticle electrode. The silver oxides may have resulted from the curing process at high temperatures as well as from the Ag nanoparticle paste itself because several of the additives can contribute to oxygen sources [24]. Because the *p*-channel PDPP-DBTE semiconductor has a deep highest occupied molecular orbital (HOMO) level of approximately −5.37 eV [22], positive charge carriers can be easily injected into the active channel from the printed Ag electrode. There are only small injection energy barrier heights of 0.2–0.4 eV which was verified from the linear output plots in the low-V_D region (see Fig. 1).

It should be noted that the thermal curing temperatures of the ROP Ag electrode on a glass (or plastic) substrate were optimized in this study at 350 °C (or 250 °C) in terms of the electrical conductivity and surface roughness of the ROP Ag electrode. The transparent and colorless (high transmittance of approximately 90%) PI plastic substrate has a sufficiently high glass transition point (T_g = 303 °C)

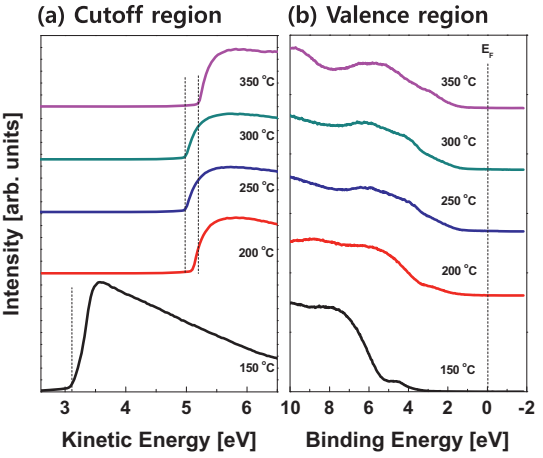

Fig. 3. Ultraviolet photoelectron spectroscopy (UPS) spectra of Ag electrode cured at different temperatures. (a) Cutoff region and (b) valence region.

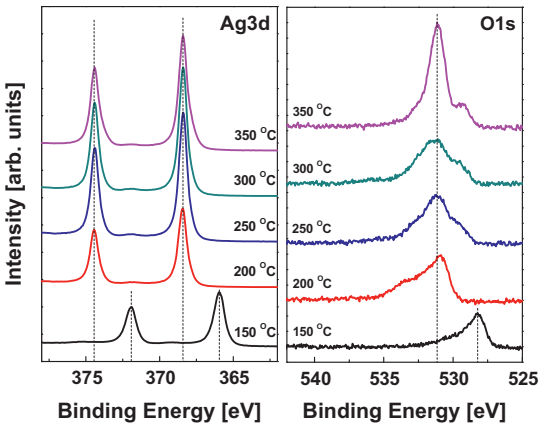

Fig. 4. X-ray photoelectron spectroscopy (XPS) spectra of Ag nanoparticle electrode cured at different temperatures.

for the high-temperature thermal curing process. The electrical characteristics of the PDPP-DBTE OFETs were evaluated as a function of curing temperatures of printed Ag S/D electrodes from 200 to 400 °C. The OFETs with ROP Ag cured at 250 °C exhibited the best electrical properties, with $\mu_{FE} = 0.18\ cm^2\ V^{-1}\ s^{-1}$, $V_T = -4.58$ V, $I_{on}/I_{off} = \sim 10^5$, and $SS = -3.57$ V dec.$^{-1}$. The OFETs with ROP Ag cured at 300 and 350 °C also exhibited similar electrical characteristics with negligible hysteresis.

In this study, printed OPTs have the same three-terminal configurations as OFETs. In the normal operating mode of an OFET, I_D through the accumulated channel is only controlled by the polarity and magnitude of the applied V_G at a given V_D. On the other hand, the control of channel conductance can be additionally enabled by the absorption of light for OPTs [25]. Fig. 5a shows the TG/BC device structure of PDPP-DBTE OPTs, where the photoresponse measurements were carried out using a bottom-illuminated Xenon arc lamp (150 W) with an optical band-pass filter with variable light intensity and wavelength. The transfer curves for printed flexible PDPP-DBTE OPTs in the dark respectively showed μ_{FE} and V_T of approximately $0.18\ cm^2\ V^{-1}\ s^{-1}$ and -0.17 V with high I_{on}/I_{off} of more than approximately 10^5. Under illuminated light at different light intensity with 3, 5, 9 and 15 mW cm^{-2}, the OPTs showed a significant increase in I_D in the region of reverse V_G between 10 and 30 V, by depending on the light intensity (see Fig. 5b). In addition, the illumination resulted in a photo-induced shift of V_T ($V_{T,ph}$) towards more positive values. The measured $V_{T,ph}$ of PDPP-DBTE OPTs was as high as 9.51 V under an light intensity of 9 mW cm^{-2}, where the initial V_T was -0.17 V in the dark. As shown in the energy-band diagram of Fig. 5c, electrons and hole carriers are efficiently photogenerated in the active channel layer, where the hole carriers easily flow to the drain electrode while electrons accumulate mostly under the source electrode. Notably, the accumulated negative carriers near the source electrode lead to a shift in V_T and can also contribute to reduce the injection barrier height for positive carrier injection from the source electrode [25]. Therefore, the lowered hole injection barrier induced by light irradiation resulted in a decrease in contact resistance and a positive shift in V_T [26].

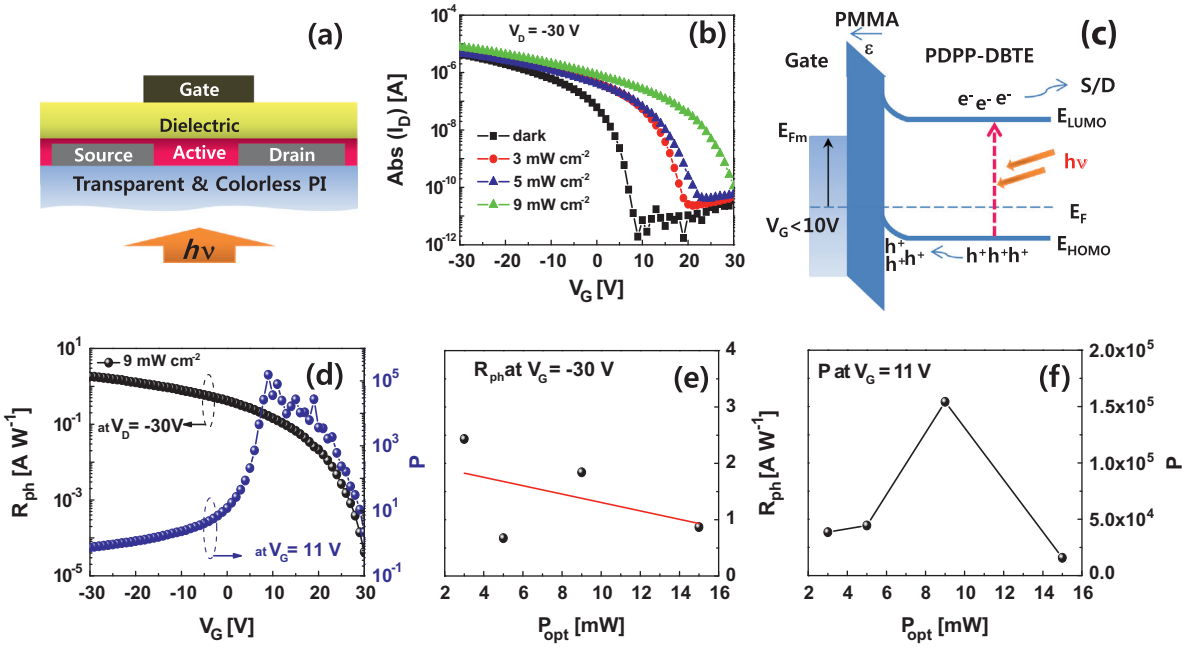

Fig. 5. (a) Device structure of flexible OPTs based on a combination of printing methods, and (b) their transfer characteristics in the dark and under illumination at different light intensity at $V_D = -30$ V. (c) Energy band diagram of the OPTs in the direction from the gate to the S/D electrodes when devices are under illumination with a negative gate bias. (d) Typical responsivity and photosensitivity of OPTs as a function of V_G. (e) The variable responsivity and (f) the photosensitivity of OPTs according to the different optical power.

The photoresponsivity and photocurrent ON/OFF ratio are the two main factors that determine the efficiency of the phototransistors. The responsivity (R_{ph}) is defined by Eq. (1), as follows:

$$R_{ph} = \frac{I_{ph}}{P_{opt}} = \frac{I_{D,ph} - I_{D,dark}}{P_{inc}A} \quad (1)$$

where I_{ph} is the photogenerated current, P_{opt} is the incident optical power, P_{inc} is the power of the incident light per unit area, and $I_{D,ph}$ and $I_{D,dark}$ are the drain currents under illumination and in the dark, respectively. A is the area of the photoactive channel region. R_{ph} reveals to what extent the optical power is converted to an electrical current. The photosensitivity (P) is defined by the signal-to-noise ratio, as shown in the following equation:

$$P = \frac{\text{signal}}{\text{noise}} = \frac{I_{ph}}{I_{dark}} = \frac{I_{D,ph} - I_{D,dark}}{I_{D,dark}} \quad (2)$$

Fig. 5d shows the typical R_{ph} and P of the printed OPT devices at light intensity of 9 mW cm^{-2}. The highest value of R_{ph} was approximately 2.5 A W^{-1} in on-state (V_G = −30 V) under an intensity of 3 mW cm^{-2}, while the highest values of P was approximately 1.54×10^5 in off-state (V_G = 11 V) under an intensity of 9 mW cm^{-2}. The R_{ph} is substantially increased with decreasing the light intensity except for 5 mW cm^{-2}, as shown in Fig. 5e. This result is consistent

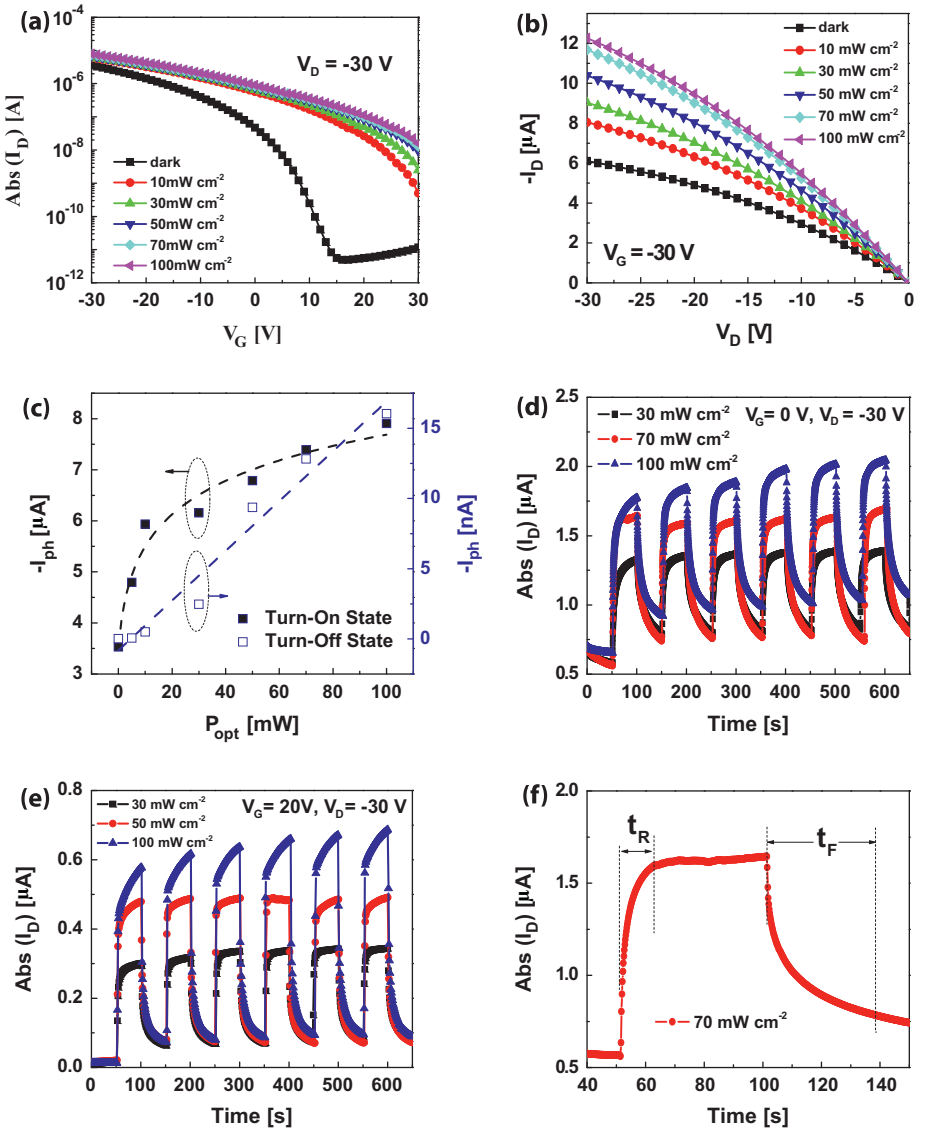

Fig. 6. (a) Transfer (at V_D = −30 V) and (b) output characteristics (at V_G = −30 V) of the PDPP-DBTE OPTs with various incident light intensity. (c) Photocurrent as a function of incident light power under turn-on (V_G = −30 V, closed squares) and turn-off (minimum I_D, open squares) states at V_D = −30 V, where the symbols denote measured data points, and the dotted lines indicate the fitted results using Eqs. (3) and (4). Time-resolved photo-response characteristics of the PDPP-DBTE OPTs upon irradiation at combinations of (d) V_G = 0 V and V_D = −30 V and (e) V_G = 20 V and V_D = −30 V. (f) Estimated response time for turn-on (t_R) and turn-off (t_F) of the light in OPTs.

with Eq. (1). Note that the illuminated light intensity was limited from 3 to 100 mW cm^{-2} in our laboratory; however, we expect the responsivity is much higher at much lower light illumination.

Fig. 6a and b shows the transfer and output characteristics, respectively, for PDPP-DBTE OPTs in the dark and under light irradiation at different light intensity from 10 to 100 mW cm^{-2}. In transfer curve, the onset and V_T are considerably shifted in the positive direction, and the magnitude of the shift and the corresponding photoinduced currents are appreciably enhanced by increasing the light intensity. The output curves in the ON state (at $V_G = -30V$) move from linear to saturation regimes. Both the slop in the linear regime and the current in the saturation regime increase with increasing illuminated light intensity. However, this increase is nonlinear, increasing rapidly at low illumination levels but beginning to saturate at higher levels [27]. This is consistent with the shifts in V_T of transfer curves. In addition, the saturation regime current exhibited V_D dependence at high P_{inc}. It is considered to be due to an increase in the photogeneration rate with drain field [27]. On the other hand, the OFF state photocurrent in transfer curves is compensated by the increase in I_D because of the shift in V_T at moment of starting the light illumination. The output characteristics in the OFF state for a linear response are not shown in this study.

As seen in Fig. 6c, the printed OPT devices were completely operated both at photovoltaic (at turn-on state, at $V_G = -30$ V) and photocurrent (turn-off state, minimum I_d) modes at $V_D = -30$ V. In photovoltaic mode, light illumination results in a $V_{T,ph}$ shift towards more positive values. When light absorption occurs, the photogenerated holes easily flow to the drain electrode, whereas electrons accumulate under the source electrode, which contributes to the $V_{T,ph}$ shift. The photocurrent caused by the photovoltaic effect, $I_{ph,pv}$, can be expressed as follows [28]:

$$I_{ph,pv} = g_m \Delta V_T = \frac{AkT}{q} \ln\left(1 + \frac{\eta q \lambda P_{opt}}{I_{pd} hc}\right) \quad (3)$$

where η is the photogeneration quantum efficiency, P_{opt} is the incident optical power, I_{pd} is the dark current for minority charges, hc/λ is the photon energy, g_m is the transconductance, ΔV_T is the threshold voltage shift, and A is a proportionality parameter. When the OPT device is in the off state, photogenerated I_D shows a linear increase with the optical power owing to a photoconductive effect. The current can be modeled according to the following equation [28]:

$$I_{ph,pc} = (q\mu_p pE)\ WD = BP_{opt} \quad (4)$$

where μ_p is the mobility of positive charge carriers, p is the charge concentration, E is the electric field in the channel, W is the gate width, D is the depth of the absorption region, and B is a proportionality factor. In Fig. 6c, various I_{ph} values are plotted as functions of the incident optical powers at the device turn-on state ($V_G = -30$ V, $V_D = -30$ V) and turn-off state (V_G was selected at the minimum I_D, with $V_D = -30$ V). The symbols denote our experimental data points, and the dotted lines indicate fitted results using Eqs. (3) and (4). The well-fitted line indicates that our PDPP-DBTE OPTs follow the photovoltaic effect in the turn-on state and the photoconductive effect in the turn-off state.

One of the very interesting advantages of organic photo detector is that the combination of themselves with organic light emitting diodes (OLEDs) and polymer elements makes it possible to realize flexible integrated components for electro-optical transceivers [4]. The potential of printed OPTs in photo detector and scanner, their photoresponse upon on-and-off switching of light were investigated. Fig. 6d and e show the time-resolved response of the PDPP-DBTE OPTs upon light irradiation with different optical powers respectively at $V_G = 0$ V and $V_G = 20$ V at the same V_D of -30 V. Obviously, the photoinduced I_D increased proportionally to the optical power. The OPT devices exhibited faster response times when light was activated (i.e., the rising time, $t_R = \sim 11.2$ s), whereas the relaxation after the deactivation of the light took place at a relatively slow rate with an exponential decay, as seen in Fig. 6f. The fast response during activation of the irradiation is attributed to the efficient photo-generation of charge carriers in PDPP-DBTE electron-rich and electron-deficient copolymer film, whereas a relatively slow recovery is believed to be mainly a result of the characteristic recombination behavior of the photogenerated charges in the active channel [29] and from the accumulated electrons near the source electrode in photovoltaic mode (turn-on state). This should be improved by the use of a pertinent semiconductor material design to allow higher detection speeds.

Flexible devices should be bendable without degradation of their electrical properties for practical applications. To evaluate the mechanical stability of printed flexible OPTs, device of 15 mm × 15 mm was laminated on the bending metal substrate with radius of 100, 80, 60, 40, 20 and 10 mm. The variation of V_T was monitored under different bending tensile strain. The calculated tensile strain due to bending ranges from 0.05% to 0.5% by following equation: Strain(%) = $1/[(2R/\Delta R) + 1] \times 100$, where R is the fixture radius, ΔR is the thickness of the bended object

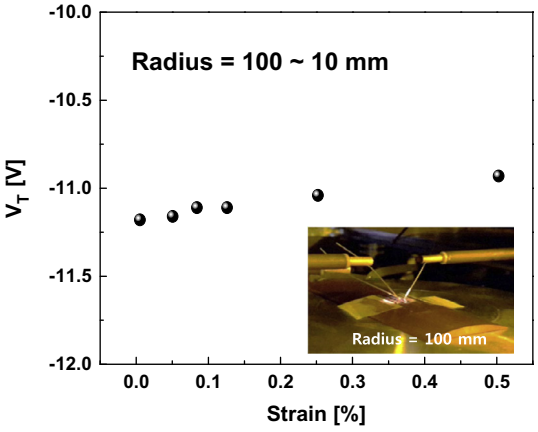

Fig. 7. Variation of V_T of flexible devices as a function of tensile strain. Inset is a digital camera image of a flexible device under mechanical bending test.

including the transparent and colorless PI substrate (100 μm), Ag electrode (450 nm), PDPP-DBTE semiconductor (50 nm), PMMA dielectric (1.2 μm), and PEDOT:PSS gate layers (50 nm). Fig. 7 shows the variation of V_T as a function of tensile strain of up to 0.5%. The device exhibited stable operation at a bending radius from 100 to 10 mm without noticeable change in V_T. Inset shows the optical image of printed flexible OPT devices under bending tensile condition. Mechanical stability of flexible devices is an essential prerequisite for the development of flexible, conformal sensors and other applications with unconventional form factors.

4. Conclusion

We have successfully demonstrated highly photosensitive OPTs on a flexible substrate using all-solution process as well as a combination of printing methods which consist of roll-to-plate reverse offset printing (ROP), inkjet printing and bar coating. Excellent electrical switching characteristics are obtained from heterogeneous interfacial properties of roll-to-plate reverse-offset-printed silver nanoparticle electrodes and inkjet-printed PDPP-DBPE polymer semiconductor. Especially, the OPTs exhibit remarkably photosensitivity with a photo-to-dark current ratio exceeding 5 orders. In addition, The OPT devices were completely operated in both at photovoltaic (at turn-on state, at V_G = −30 V) and photocurrent (turn-off state, minimum I_d) modes at V_D = −30 V. We studied both theoretically and experimentally the optoelectronic properties of the combinational printed OPTs, and confirmed comparable tendency. Outstanding mechanical stability, in addition, is observed with up to 0.5% of strain applied to the flexible OPTs. Hence, by manufactured with a combination of various GAP methods such as roll-to-plate ROP, inkjet printing and bar coating, these devices are very promising candidates for large-area and low-cost flexible optoelectronics applications.

Acknowledgements

This work was supported by the IT R&D program of MKE/KEIT (Grant No. 10041416, The core technology development of light and space adaptable new mode display for energy saving on 7inch and 2 W), and we thank the staff of KBSI for technical assistance. This research was partially supported by a grant (code no. 2011-0031639) from the Centre for Advanced Soft Electronics under the Global Frontier Research Program of the Ministry of Education, Science and Technology (MEST), a grant (code No. 13-12-N0101-41) from the Primary Research Program of Korea Electrotechnology Research Institute (KERI).

References

[1] Y. Yang, R.C. da Costa, M.J. Fuchter, A.J. Campbell, Nat. Photonics 7 (2013) 634.
[2] T.P.I. Saragi, T. Spehr, A. Siebert, T. Fuhrmann-Lieker, J. Salbeck, Chem. Rev. 107 (2007) 1011.
[3] M.E. Gemayel, M. Treier, C. Musumeci, C. Li, K. Müllen, P. Samorì, J. Am. Chem. Soc. 134 (2012) 2429.
[4] K.-J. Baeg, M. Binda, D. Natali, M. Caironi, Y.-Y. Noh, Adv. Mater. 25 (2013) 4267.
[5] C.A. Di, F.J. Zhang, D.B. Zhu, Adv. Mater. 25 (2013) 313.
[6] Y. Guo, G. Yu, Y. Liu, Adv. Mater. 22 (2010) 4427.
[7] D.A. Pardo, G.E. Jabbour, N. Peyghambarian, Adv. Mater. 12 (2000) 1249.
[8] D. Khim, H. Han, K.-J. Baeg, J. Kim, S.-W. Kwak, D.-Y. Kim, Y.-Y. Noh, Adv. Mater. 25 (2013) 4302.
[9] Y.-Y. Noh, N. Zhao, M. Caironi, H. Sirringhaus, Nat. Nanotechnol. 2 (2007) 784.
[10] T. Mäkelä, S. Jussila, H. Kosonen, T.G. Bäcklund, H.G.O. Sandberg, H. Stubb, Synth. Met. 153 (2005) 285.
[11] H. Yan, Z. Chen, Y. Zheng, C. Newman, J.R. Quinn, F. Dötz, M. Kastler, A. Facchetti, Nature 457 (2009) 679.
[12] D. Zielke, A.C. Hübler, U. Hahn, N. Brandt, M. Bartzsch, U. Fügmann, T. Fischer, J. Veres, S. Ogier, Appl. Phys. Lett. 87 (2005) 123508.
[13] K.-J. Baeg, J. Kim, D. Khim, M. Caironi, D.-Y. Kim, I.-K. You, J.R. Quinn, A. Facchetti, Y.-Y. Noh, ACS Appl. Mater. Interfaces 3 (2011) 3205.
[14] G.H. Gelinck, H.E.A. Huitema, E.V. Veenendaal, E. Cantatore, L. Schrijnemakers, J.B.P.H.V.D. Putten, T.C.T. Geuns, M. Beenhakkers, J.B. Giesbers, B.-H. Huisman, E.J. Meijer, E.M. Benito, F.J. Touwslager, A.W. Marsman, B.J.E.V. Rens, D.M.D. Leeuw, Nat. Mater. 3 (2004) 106.
[15] A. Hübler, B. Trnovec, T. Zillger, M. Ali, N. Wetzold, M. Mingebach, A. Wagenpfahl, C. Deibel, V. Dyakonov, Adv. Energy Mater. 1 (2011) 1018.
[16] K.-J. Baeg, D. Khim, J. Kim, B.-D. Yang, M. Kang, S.W. Jung, I.-K. You, D.-Y. Kim, Y.-Y. Noh, Adv. Funct. Mater. 22 (2012) 2915.
[17] R. Rotzoll, S. Mohapatra, V. Olariu, R. Wenz, M. Grigas, K. Dimmler, O. Shchekin, A. Dodabalapur, Appl. Phys. Lett. 88 (2006) 123502.
[18] T. Pal, M. Arif, S.I. Khondaker, Nanotechnology 21 (2010) 325201.
[19] Y.-H. Kim, J.-I. Han, M.-K. Han, J.E. Anthony, J. Park, S.K. Park, Org. Electron. 11 (2010) 1529.
[20] M. Kim, J.B. Koo, K.-J. Baeg, S.-W. Jung, B.-K. Ju, I.-K. You, Appl. Phys. Lett. 101 (2012) 133306.
[21] T.K. An, I. Kang, H.-J. Yun, H. Cha, J. Hwang, S. Park, J. Kim, Y.J. Kim, D.S. Chung, S.-K. Kwon, Y.-H. Kim, C.E. Park, Adv. Mater. 25 (2013) 7003.
[22] I. Kang, T.K. An, J.-A. Hong, H.-J. Yun, R. Kim, D.S. Chung, C.E. Park, Y.-H. Kim, S.-K. Kwon, Adv. Mater. 25 (2013) 524.
[23] Y. Sun, Y. Xia, Science 298 (2002) 2176.
[24] D. Kim, S. Jeong, H. Shin, Y. Xia, J. Moon, Adv. Mater. 20 (2008) 3084.
[25] G. Horowitz, J. Mater. Res. 19 (2004) 1946.
[26] Y.F. Xu, P.R. Berger, J.N. Wilson, U.H.F. Bunz, Appl. Phys. Lett. 85 (2004) 4219.
[27] X. Wang, K. Wasapinyokul, W. De Tan, R. Rawcliffe, A.J. Campbell, D.D.C. Bradley, J. Appl. Phys. 107 (2010) 024509.
[28] H.S. Kang, C.S. Choi, W.Y. Choi, D.H. Kim, K.S. Seo, Appl. Phys. Lett. 84 (2004) 3780.
[29] T.P.I. Saragi, R. Pudzich, T. Fuhrmann, J. Salbeck, Appl. Phys. Lett. 84 (2004) 2334.